Improving Sensor Fusion: A Parametric Method for the Geometric Coalignment of Airborne Hyperspectral and Lidar Data

Maximilian Brell, Christian Rogass, Karl Segl, Bodo Bookhagen, and Luis Guanter

Abstract—**Synergistic applications based on integrated hyperspectral and lidar data are receiving a growing interest from the remote-sensing community. A prerequisite for the optimum sensor fusion of hyperspectral and lidar data is an accurate geometric coalignment. The simple unadjusted integration of lidar elevation and hyperspectral reflectance causes a substantial loss of information and does not exploit the full potential of both sensors. This paper presents a novel approach for the geometric coalignment of hyperspectral and lidar airborne data, based on their respective adopted return intensity information. The complete approach incorporates ray tracing and subpixel procedures in order to overcome grid inherent discretization. It aims at the correction of extrinsic and intrinsic (camera resectioning) parameters of the hyperspectral sensor. In additional to a tie-point-based coregistration, we introduce a ray-tracing-based back projection of the lidar intensities for area-based cost aggregation. The approach consists of three processing steps. First is a coarse automatic tie-point-based boresight alignment. The second step coregisters the hyperspectral data to the lidar intensities. Third is a parametric coalignment refinement with an area-based cost aggregation. This hybrid approach of combining tie-point features and area-based cost aggregation methods for the parametric coregistration of hyperspectral intensity values to their corresponding lidar intensities results in a root-mean-square error of 1/3 pixel. It indicates that a highly integrated and stringent combination of different coalignment methods leads to an improvement of the multisensor coregistration.**

Index Terms—**Airborne laser scanning (ALS), coregistration, direct georeferencing, imaging spectroscopy, multisensor, parametric georeferencing, preprocessing, ray tracing, rigorous geocoding, sensor alignment, sensor fusion.**

I. INTRODUCTION

DATA fusion is a common method for the improvement of data quality and information content in remote-sensing

M. Brell, C. Rogass, K. Segl, and L. Guanter are with the Helmholtz Centre Potsdam GFZ German Research Centre for Geosciences, 14473 Potsdam, Germany (e-mail: brell@gfz-potsdam.de).

B. Bookhagen is with the Institute of Earth and Environmental Science, University of Potsdam, 14476 Potsdam, Germany.

measurements. A challenging example is the fusion of airborne hyperspectral and lidar data, which allows integrating high spectral resolution with high-resolution spatial information. The fusion of both data types, with the purpose of completing or enhancing a comprehensive object characterization, is important and promising, particularly for heterogeneous environments [1] and steep terrain. Different studies have already proven the potential of integrating lidar and hyperspectral imaging (HSI) data for various areas of research, including urban [2], [3], forest [4]–[8], and ecological applications [5], [9], [10]. For data analysis and classification procedures, the elevation information serves as an additional dimension to enhance information content and classification results.

An overall prerequisite and therefore one of the most important steps for proper data fusion is the accurate geometric coregistration or coalignment of both sensor entities. For example, a misalignment between lidar and HSI sensors of ±3-pixel root mean square (RMS) in both X and Y directions leads to a significant reduction of data information content, depending on the heterogeneity of the mapped targets [1]. Therefore, a proper geometric coalignment of both sensors is indispensable for accessing the entire information content of both data entities. Additionally, a perfect coalignment is also a precondition for a radiometric, spectral, and spatial fusion of HSI and lidar sensors. Standard direct geometrical preprocessing of HSI data under practical and nonoptimized conditions result in absolute geometric accuracy of 1–3 pixels [11]. Therefore, HSI systems often do not meet the spatial requirements of applications concerning accuracy and resolution. This is caused by variable and intrinsic optical aberrations in the sensor design and the lack of standardized data preprocessing workflows. In comparison to that, the geometric accuracy of modern lidar systems is significantly higher. They can reach vertical accuracies of smaller 20 cm [12] and horizontal accuracies of a few decimeters, depending on the flight parameters, the preprocessing, the terrain slope, and the reflectivity of the targets. Often, the lidar data are taken as a geometric reference for the spatial fusion with HSI data.

Standard fusion of HSI and lidar is limited by the integration of the separated data entities, the gridded hyperspectral data cube (X, Y, spectrum), and the gridded digital elevation model (X, Y, Z). Usually, both data entities are generated in separated preprocessing workflows. The gridded elevation

model is only considered during the direct geocoding [11], [13] and atmospheric correction [14] of the HSI data. A proper geometric coalignment is assumed but not explicitly performed. In contrast, advanced fusion approaches include a geometrical coalignment procedure as a central preprocessing step. There exist many variations because the broad term fusion for lidar and HSI data is indefinite and does not implicate a standardized method or level of implementation. In general, existing fusion approaches share the aim of enhancing the information content but differ by the chosen level of implementation and method. Physical or empirical fusion methods are applied to different data or product levels [15]. For the geometric coalignment of lidar and hyperspectral data, various methods exist, and they can be distinguished into parametric (physical) and non-parametric (empirical) approaches. Nonparametric approaches attempt to compensate the geometric errors by adjusting the preprocessed gridded data sets during postprocessing. They employ area-based or feature-based detection algorithms in both data entities and perform an interpolation or resampling-based rectification to a common image plane [3], [16]. In general, nonparametric approaches require sufficient, homogeneous distributed, and detectable objects or intensity gradients in both scenes. In particular, for low-contrast and homogeneous scenes, these requirements are not fulfilled and result in rubber-sheeting problems between the detected objects. Therefore, area-based nonparametric intensity methods [17] are very sensitive to illumination and spatial response differences, which are inherent in lidar and HSI images. In contrast, parametric approaches try to minimize the systematic error budget during the data preprocessing procedure. They need background information for sensor parameters, positioning, and attitude, in addition to the raw sensor data [1]. Parametric coalignment strategies attempt to assign generally valid offset parameters (see Table II: overview of parameters optimized in the coalignment approach) to the global parametric geocoding procedure [8]. These offset parameters are determined by minimizing the distances between local features, which are detectable in a small subset of both overlapping sensor data sets. Therefore, parametric methods are less influenced by their respective radiometric response of the sensors, and an additional extensive radiometric adaptation is not imperative. Hence, they are well suited for the fusion of active and passive sensors enabling a separate geometric and radiometric fusion. However, since parametric approaches are tie-point based and usually carried out on a pixel level, they do not completely describe the geometric fit of more complex features. Altogether, the gridded integration or comparison of both data entities is limited and not ideal for high geometric accuracies because it results in spectral and spatial discretization and, therefore, in a substantial information loss [18].

The aim of this paper is to develop a coalignment method avoiding the known drawbacks of parametric and nonparametric methods, which can simultaneously handle the inherent geometric drawbacks of hyperspectral sensors and different sensor responses without rasterized discretization. This results in a novel approach for the improved geometric fusion of HSI sensors and lidar sensors starting at a sensor-driven data level. The key element is the definition and implementation of a robust parametric coalignment procedure to minimize the inherent error budget of the HSI sensor in relation to the lidar intensity data. Our developed hybrid approach integrates an area-based cost aggregation often used in nonparametric approaches into a parametric approach often limited to feature-based alignment. It is based on the main software modules of the in-house software "HyPrepAir," which are developed for hyperspectral airborne preprocessing.

II. General HSI and Lidar Sensor System Characteristics

Both sensor systems differ fundamentally in their function and data collecting principles. HSI systems are passive sensors collecting electromagnetic solar irradiation reflected from the earth surface toward the sensor. HSI systems can measure reflected radiance in the visual-to-near-infrared (400–1000 nm VNIR) and short-wave-infrared domain (1000–2500 nm SWIR). The high spectral resolution of the HSI sensor results in an almost continuous spectrum [19], [20]. In contrast, lidar systems are active sensors emitting pulsed radiation of one narrow bandwidth toward the earth surface (see left in Fig. 1). Lidar systems usually emit and receive very narrow monochromatic wavelength ranges of 532, 1064, or 1550 nm. The reflected radiation intensity, as well as the time of flight, of the laser pulse is measured. A 3-D point cloud (X, Y, Z) with the intensity values of the reflected laser pulses is the result. Both sensors potentially operate in the visible and infrared wavelength domain and share an overlapping wave-length range (see right in Fig. 1). This overlapping wave-length range is the main linkage between both sensor systems and the basic requirement of the developed parametric-based coregistration.

The bandwidth of the lidar impulse is very short in comparison to bandwidths of the HSI [5–20 nm full-width at half-maximum (FWHM)]. A Gaussian spectral response function (SRF) with the intensity maximum in the center of the function can be assumed for every band of both sensors [20].

Modern HSI systems are usually designed as pushbroom scanners because of longer integration times that improve their signal-to-noise ratio (SNR) of the data. The recorded reflected radiation per scanline is dispersed by a grating or prism into spectral fractions and thereby projected to discrete rows of the full-frame sensor array [19]. The geocoding procedure follows the collinearity relations [11], [13]. Based on the attitude and position of the airplane measured by the global position system (GPS) and the inertial measurement unit (IMU) at a given point in time, each image pixel can be geocoded with its pointing characteristics. These characteristics are also affected by nonuniformities in the spatiospectral frames of the pushbroom imaging spectrometer called keystone [21], [22] and smile [21] effects.

The lidar sensor is a whiskbroom system. A rotating mirror is deflecting the emitted laser pulses in varying angles and high repetition rates (up to 400 kHz) in the direction of the earth surface. A receiver measures the reflected intensity and its chronological sequence (full waveform) [23], [24].
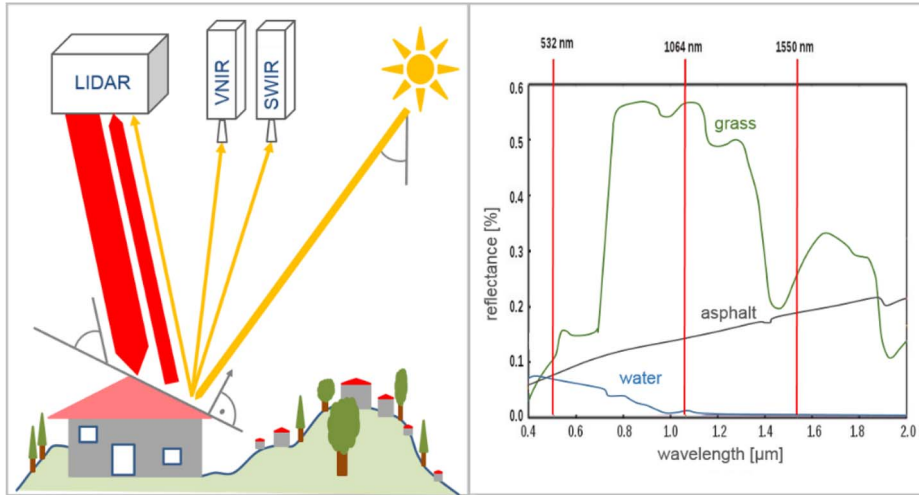
Fig. 1. (Left) Different radiation models for the sensors and (right) possible wavelength overlaps between lidar and HSI systems. Red vertical lines show common laser wavelengths drawn over characteristic spectra for grass (green), asphalt (black), and water (blue).

The direction and duration of every laser impulse, in combination with the attitude and position of the sensor, enable the calculation of the location and distance of the reflecting surface.

A. Spatial Sampling Characteristics

Due to the different sensor designs, the spatial data acquisition results in different sampling distributions and sampling densities. Lidar systems have a wide field of view (FOV; $< 60°$). During one mirror rotation, up to $400\,000$ pulses with a short delay in time are emitted. The movement of the airplane causes a shift of every lidar point. The sampling density decreases with off-nadir direction, which is compensated by overlapping flight stripes. The laser beam has a small divergence of less than 0.5 mrad, which results in altitude-dependent footprint diameters [23], [24]. The generated point density and ground sampling distance (GSD) are dependent on the flight speed above ground and the altitude of the airplane.

HSI sensors usually have a smaller FOV and, therefore, a narrow swath. The GSD between every pixel center in a sensor row is defined by the instantaneous FOVs (IFOVs) in the across- and along-track directions, the time frame between two scanlines, flight speed, and attitude [20]. The IFOVs and the pointing of the sensor elements are not regular due to the sensor design and sensor motion. This results in an irregular pointing in the across- and along-track direction [20]. The high spectral resolution of the HSI sensor is at the expense of the spatial resolution and accuracy. VNIR and SWIR sensors are often designed as separated sensors. SWIR sensors have a lower spectral and sometimes spatial resolution than VNIR sensors because of the significantly reduced radiance in the SWIR wavelength range. The sampling distribution of the pushbroom sensor is more regular compared to the whiskbroom lidar sensor because one entire scanline is measured simultaneously [20]. In summary, the initial spatial sampling distribution patterns generated by airborne lidar and HSI sensors are completely different and irregular and have to be resampled onto regular grids for further processing.

B. Challenge of the Geometric Coregistration

Sensor model, position and attitude accuracy (IMU/GPS), and alignment errors (lever arm, boresight, and synchronization) are the main error sources influencing the geometric alignment. Fig. 3 shows the scheme of the system integration and the inherent alignment errors. The boresight offset (offset angle introduced by the dislocation of the image projection center and the IMU origin of coordinates) and the lever arm (dislocation between the GPS antenna and the IMU origin of coordinates) have to be corrected for every sensor, separately. All sensors are dependent on the delivered IMU/GPS accuracy, which also introduces geometric errors to the lidar and HSI data. Due to their complicated sensor design and their passive character described earlier, HSI sensors have certain drawbacks (strong central perspective, keystone, lower spatial resolution, etc.) in comparison with geometrically highly specialized lidar sensors. Additionally, HSI sensors are usually geometrically and spectrally calibrated under laboratory conditions [25]–[27]. However, under practical flight conditions, pressure and temperature change, and vibration and accelerations influence the sensor geometry to a certain degree. Because of the large distances between target and sensor, even small distortions lead to conspicuous spatial aberrations that affect the coalignment of the sensors.

The physical linkage between spatial and spectral domains of both sensor responses has to be considered for sensor fusion [28]. The adaptation of the different spatial and spectral responses of the sensors is the main challenge. These response differences are clearly recognizable by comparing the intensity images in the overlapping wavelength of the lidar sensor (see left in Fig. 4) with the intensity images of the SWIR sensor (see right in Fig. 4). A radiometric calibration of the lidar intensities itself is not performed yet, because the differences of the intensities are dominated by the passive character of the
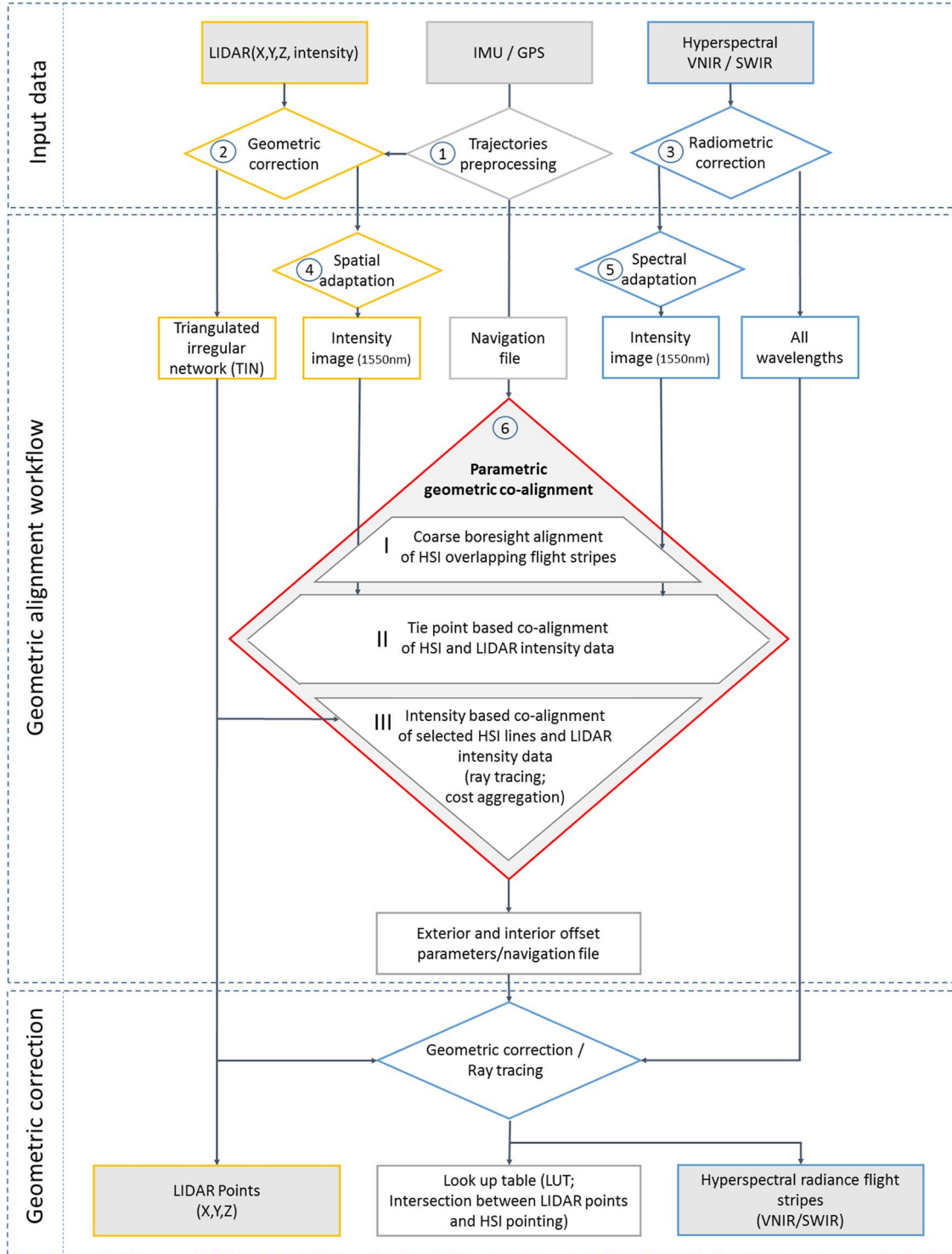
Fig. 2. Overview of the simplified geometric fusion workflow (rectangles represent data products; rhombs represent processing procedures; the lidar part is outlined in yellow; central linkage based on IMU/GPS data are outlined in gray; the HSI part is outlined in blue; the central fusion step is outlined in red). The trajectories are the key linkage in the fusion workflow, and therefore, their preprocessing is the first step.

HSI intensities. Hence, the developed geometric coalignment procedure should be robust enough to operate independent of a cross-calibration. Altogether, the complete coalignment should avoid unnecessary resampling procedures to conserve the original data quality. In addition, the large data amount is an additional challenge that has to be handled efficiently to enable preprocessing of large flight campaigns.

III. METHOD

The developed method for in-flight geometrical alignment of airborne hyperspectral and lidar intensity data can be separated into three principle parts (see Fig. 2):
- input data generation and preprocessing of the input data;
- geometric alignment workflow;
- geometric correction.

It includes the in-flight airborne sensor integration and data acquisition strategy, as well as the geometric coalignment approach itself. After data acquisition and preprocessing of the lidar and HSI data, a spectral and spatial response adaptation (see rhombs 4 and 5 in Fig. 2) is realized. The parametric coregistration itself is a three-step alignment procedure (see rhomb 6 in Fig. 2) based on optimizing extrinsic and intrinsic alignment parameters. In a first step, a coarse tie-point-based coalignment of overlapping HSI stripes is realized. The second step coaligns the HSI image to the lidar intensity image with the use of tie points. The third step is an intensity- and area-based cost aggregation. This method compares the template HSI intensities of three sensor rows with the corresponding lidar intensities calculated for different offset parameters. The corresponding lidar intensities are generated by a ray-tracing-based geometric intersection of the HSI sensor element pointing, which is represented by a cone, with the lidar point cloud. The geometric correction is the final procedure, which assigns the determined offset parameters to the complete flight campaign. In the following, the three principle parts and their respective processing procedures are described in detail.

A. Input Data Generation

For input data generation, the airborne sensor integration and data acquisition strategy has to be adopted to ensure proper data quality. Additionally, the preprocessing part of the workflow (see rhombs 1–3 in Fig. 2) homogenizes the sensor outputs of the three different sensors to a data level, which can be used as a starting point for the determination of the global extrinsic and intrinsic alignment parameters (see Table II).

1) Airborne Sensor Integration and Data Acquisition: For the development and testing of a geometric fusion algorithm, a calibration flight campaign was realized. A HySpex VNIR-1600 [29] and a HySpex SWIR-320m-e [29] HSI sensor, in combination with a lidar LMS-Q560 [30], were integrated inside a Cessna 207 Skywagon.

Table I gives an overview of the particular sensor parameters. An AEROcontrol-IId IMU with available data rates of 256 Hz, in combination with a NovAtel OEM4-G2 GPS receiver, was used for measuring the position and attitude of the airplane. The provided accuracy of position and attitude by the IMU/GPS is essential for the direct georeferencing of the sensors. The IMU is able to deliver postprocessing accuracies of $0.004°$ RMS for roll and pitch and $0.01°$ RMS for heading.

Measurement setup, sensor operation, and flight planning were adapted with the objective of generating an ideal data basis for a proper sensor fusion. The HSI (VNIR, SWIR), lidar, and differential GPS (DGPS)/IMU sensors were arranged on a passive damped aluminum plate. Their origins of ordinates were installed as close together as possible (see Fig. 3). A static connection is established between the three sensors to avoid vibrations and spatial distortions between the sensors.

The test flight generated about 16 GB of HSI image data and about 1 GB of lidar point data (21×10^6 points). The data set consists of four flight lines (see Fig. 4) flown 800 m above ground over an airfield bordering suburban development in Kamenz (Germany, $51.29063°$ N $14.12107°$ E). The terrain

TABLE I
OVERVIEW OF USED SENSORS AND PARTICULAR PARAMETERS

|	Lidar (LMS-Q560)	VNIR and SWIR HSI (Hyspex)
Principle	active	passive
Sensor design	Whiskbroom (polygon mirror)	Pushbroom
FOV (Field of View)	60°	VNIR: 35.5° SWIR: 27.2°
IFOV (instantaneous field of view)	-	VNIR: across track 0.18 mrad along track 0.36 mrad SWIR: across track 0.75 mrad along track 0.75 mrad
Laser beam divergence	< 0.3 mrad	
Spectral range	1550 nm	VNIR: 400 - 1000 nm SWIR: 1000 − 2500 nm
Frames per second (HSI) Pulse frequency (lidar)	240 kHz (160 lines/s)	VNIR: 135 fps SWIR: 100 fps
Spectral sampling	monochromatic	VNIR: 3.7 nm SWIR: 6 nm
Pulse length	< 4ns	
FWHM (spectral)		VNIR: 1.0-2 pixel SWIR: 1.5-2 pixel
Spectral bands	1; Full Waveform	VNIR: 160 SWIR: 256
Spatial pixels hyperspectral		VNIR: 1600 SWIR: 320
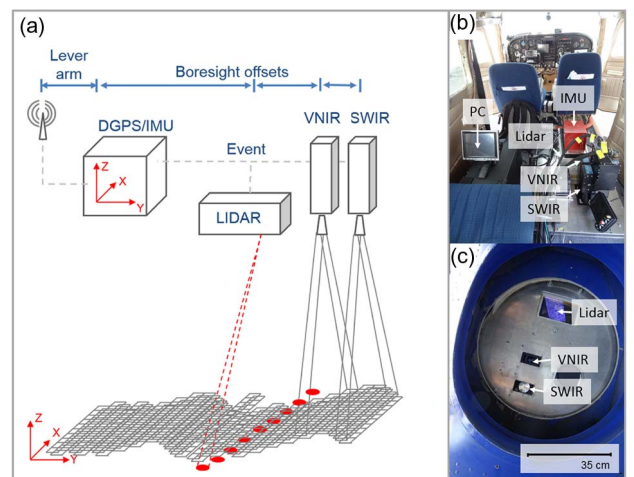
Fig. 3. (a) Scheme of airborne sensor integration and function principle (DGPS: differential GPS; IMU: initial measurement unit). (b) Photo of sensor integration in the airplane and (c) photo of sensor integration below the airplane.

is relatively flat with a height range of 33 m. The heterogeneous suburban objects (buildings, roads, trees, and fields) introduce most of the elevation changes, generating slopes up to $90°$

This article has been accepted for inclusion in a future issue of this journal. Content is final as presented, with the exception of pagination.

6   IEEE TRANSACTIONS ON GEOSCIENCE AND REMOTE SENSING
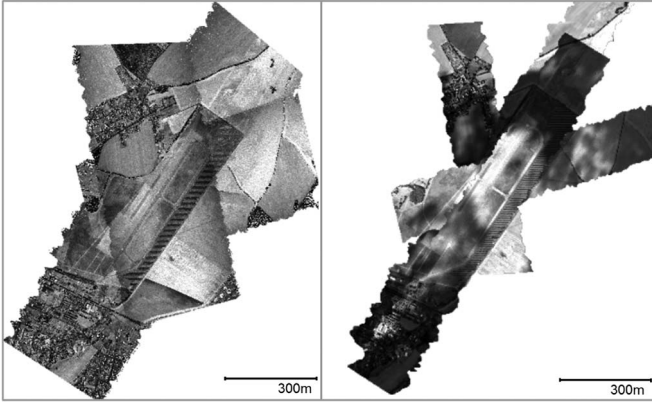

Fig. 4. Geocoded overview of the four flight lines: (left) lidar intensity image (1550 nm) and (right) HSI SWIR intensity image (1550 nm).

between surface objects. The flight altitude and the flight speed of about 190 km/h above ground result in a ground sampling resolution of about 1.5 m for SWIR and 0.8 m for VNIR. The lidar scanner generates a point density of about 5 points/m^2 in nonoverlapping areas (100 lines per second, 150 kHz, and 60° FOV parameterization).

2) Preprocessing of HSI, Lidar, and DGPS/IMU Data: The preprocessing part of the data generated by the three sensors ensures the homogenization and provision of the required input data quality.

a) Trajectory preprocessing: The parametric geocoding of the lidar and the HSI is based on the trajectories of the airplane that define the orientation and line of sight of the sensors. The trajectories are generated by combining the binary information of the position (GPS) and attitude (IMU). The differential postprocessing (see rhomb 1 in Fig. 2) of the DGPS signal is realized by using phase and Doppler measurements of a nearby ground reference station with the software GrafNav. The offset between the GPS antenna and the IMU origin of ordinates (lever arm) is corrected. High accuracy is guaranteed by integrating the DGPS with the IMU information. Both error dynamics are uncorrelated. Forward and reverse Kalman filtering is done in the postprocessing procedure to minimize both errors. The trajectory preprocessing was done with the software AeroOffice. The trajectory optimization results in smooth best estimation trajectories for the IMU/GPS origin of ordinate with state-of-the-art accuracy for position (X0, Y0, Z0) and attitude (roll, pitch, and heading). The output ASCII file provides the base of the direct geocoding of both sensors.

b) Lidar geometric preprocessing: The geometric alignment workflow of the two sensors is based on an iterative coregistration of the HSI data to the lidar intensity data. Therefore, the geometric preprocessing of the lidar data (see rhomb 2 in Fig. 2) has to create accuracies that are high enough to serve as a geometric reference. This is achieved by a state-of-the-art geometric correction workflow, including boresight alignment, single-flight stripe correction, and relative flight stripe adjustment, implemented in the software RiPROCESS. Their overall strategy is to minimize the lidar inherent random and systematic error budget (instrument errors, trajectory errors, synchronization errors, and atmospheric conditions). The resulting lidar point cloud is filtered with the software Terrasolid. Erroneous
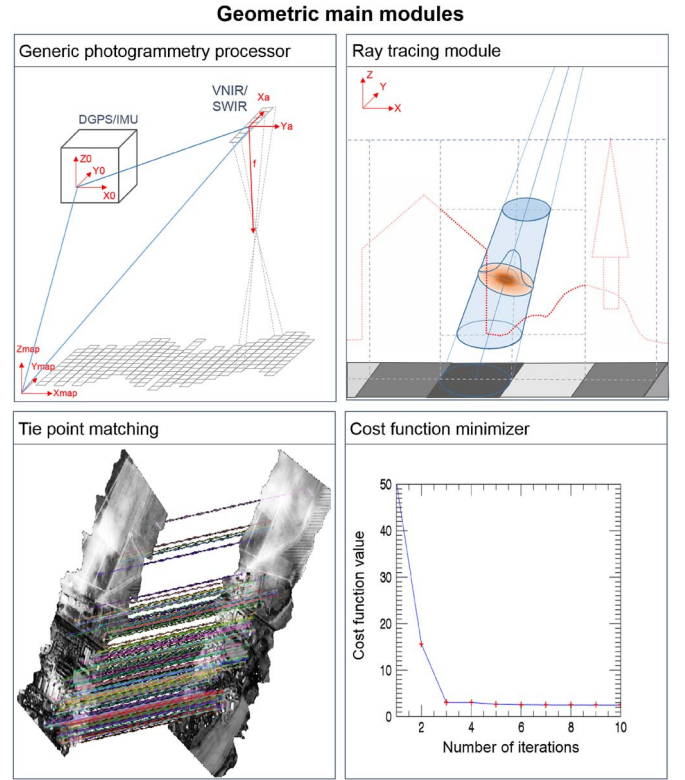

Fig. 5. Four main geometric modules, which are used across the developed geometric alignment procedure.

lidar point outliers inside the point cloud are removed by analyzing the height and spatial-neighborhood relationships. This robust outlier removal enables an optimized geometric representation of the surface features. The resulting corrected 3-D point cloud ensures very high positional accuracies. The backscattered lidar intensity information of the 3-D points is subsequently used (see Section III-B1b) for generating a gridded true orthoimage. The 3-D point cloud itself is used as morphometric surface and elevation information. This point cloud is divided into regular spatial tiles, which are stored as separated files in the LASer (LAS) format.

c) Hyperspectral image preprocessing: In a first step of the hyperspectral preprocessing, a radiometric correction (see rhomb 3 in Fig. 2) is applied to transform digital numbers into at-sensor-radiance values. The radiometric correction is accomplished by applying a linear transformation with determined calibration coefficients (offset and gain) to every image pixel. The offset (that includes the thermally induced dark current) is determined automatically, by closing a shutter before (VNIR) or after (SWIR) every flight line [27], measuring the dark signal. The gain coefficient is determined in laboratory, measuring the sensor's response of a radiance standard that is illuminated by a known artificial light source [31]. The result of the radiometric correction is a separate hyperspectral data cube for VNIR and SWIR, including at-sensor-radiance values.

B. Geometrical Coalignment Method

The geometric alignment and geocoding procedure consists of four main modules (see Fig. 5): a generic photogrammetry

This article has been accepted for inclusion in a future issue of this journal. Content is final as presented, with the exception of pagination.

BRELL *et al.*: IMPROVING SENSOR FUSION: PARAMETRIC METHOD FOR GEOMETRIC COALIGNMENT OF DATA

7

processor, a ray tracing module, an automatic robust tie-point matching algorithm, and a cost-function minimizer.

The central component of the geometric workflow is a generic photogrammetric processor that transforms the image coordinates (Xa, Ya) into map coordinates (Xmap, Ymap). This module is closely linked to a ray tracing module that calculates the elevation (Zmap) on the lidar point cloud. The direct rigorous parametric geocoding is performed based on the generated trajectories, focal length, and principle point, following the principles of the collinearity equation that define the transformation between the pushbroom scanline image space and the object space. Based on the collinearity equation, the object coordinates of every HSI sensor element at the minimum elevation (Zmap) projection plane is calculated. The position and attitude for every exposed sensor row are tapped on demand from the original navigation file in its full temporal resolution with subrow precision. A rigid assignment of a fixed position and attitude with discretization to integral sensor rows is avoided during the alignment and georeferencing process. This ensures synchronization optimization between sensor and DGPS/IMU as well as subpixel matching opportunity based on the original navigation data.

The ray tracing module defines the geometric intersection (Xmap, Ymap, Zmap) of the HSI pointing with the lidar point cloud. In addition, the ray tracing module calculates the lidar points inside a projected cone and their distance to the cone center. The cones represent the pointing of an HSI pixel. The ray tracing module is always performed subsequent to the photogrammetry processor and with the same procedure. The minimum and maximum elevation projection planes define 3-D line vectors representing the HSI pointing. These 3-D line vectors are shortened iteratively to minimize the potentially neighboring lidar points. For elevation determination, the intersection between this 3-D vector line and a triangulated irregular network (TIN) generated from the 3-D lidar point cloud is calculated. This is based on a fast triangle line intersection test using barycentric coordinates. The lidar points inside a cone and their distance to the cone center are calculated by defining the cone with the across- and along-track IFOV of the respective sensor pixel. The lidar points inside each cone, representing the respective HSI pixel lines of sight, are indexed and stored in a lookup table (LUT). Overall, the space partitioning procedure inside the ray tracing module that handles the point cloud is realized by a 3-D histogram-based voxel filter.

An automated tie-point determination and matching algorithm is required at several processing steps. The developed tie-point detection and matching algorithm is based on an established robust feature detector called scale-invariant feature detection (SIFT) developed by Lowe [32]. The key point detector is based on finding the local maxima in differences of Gaussians between adjacent scales. The SIFT key point descriptor vectors are based on gradient histograms of the detected feature points. SIFT tie points are assumed to be scale, rotation, and transformation invariant [32]. The applied feature matching is based on the minimum Euclidean distance of the descriptor vectors. The feature matching is adapted to the specific sensor characteristics of both sensors concerning masking, maximum spatial match radius, and location. The detected

TABLE II
OVERVIEW OF PARAMETERS OPTIMIZED IN THE COALIGNMENT APPROACH

Parameter type	Parameter name	Abbreviation	Co-alignment step		
			1	2	3
Extrinsic parameters	Roll		x	x	x
	Pitch		x	x	x
	Heading		x	x	x
	Altitude	Z0		x	x
	Synchronization timing	Δt		x	
Intrinsic parameters	Principal point	X0a, Y0a		x	x
	Focal length	f		x	x

tie points are filtered based on the perspective transformation model between the two involved images with random sample consensus (RANSAC) [33]. Thus, false matches can be robustly removed.

For the parametric coregistration of the HSI data to the lidar data, a cost-function minimization is essential to improve various extrinsic and intrinsic parameters (see Table II) to enhance the average accuracy. Two different cost minimization strategies are involved. A tie-point-based approach and an area-based approach. The area-based approach is explained in Section III-B2c. For the tie-point-based version approach, the parameters of the collinearity equations are iteratively modified by bisecting the offset parameter intervals. This is realized by varying the involved parameters of the hyperspectral sensor for every single tie-point pair. For every iteration, the pointing directions are calculated parallel for the respective parameter intervals by the photogrammetry processor. The intersections with the lidar point cloud are calculated by the ray tracing module. The parameter offset which generates the smallest 3-D RMS error (RMSE) between the corresponding tie points in the object space is the final offset parameter. The respective starting parameter range and interval size are predefined by the sensor system and integration.

1) Adjustment of the Sensor Concerning Spectral and Spatial Responses: One of the essential steps for the fusion of the two sensors is the adaptation and homogenization of the different spectral and spatial sensor responses, in order to make them comparable [34], [35]. Due to different spectral and spatial resolutions, the HSI wavelength and bandwidth is adapted to the lidar specification, whereas the irregular lidar point intensities are adapted spatially to the HSI response.

a) Spectral response adaptation: The spectral response adaption (see rhomb 5 in Fig. 2) usually comprises a spectral upsampling of the HSI using interpolation [36] and a convolution with the assumed SRF of the lidar data [21]. Due to the fact that the spectral bandwidth of one lidar pulse is extremely short, the FWHM of the lidar SRF was expected to be close to zero. Thus, the corresponding HSI intensity with the 1550-nm

This article has been accepted for inclusion in a future issue of this journal. Content is final as presented, with the exception of pagination.

8   IEEE TRANSACTIONS ON GEOSCIENCE AND REMOTE SENSING
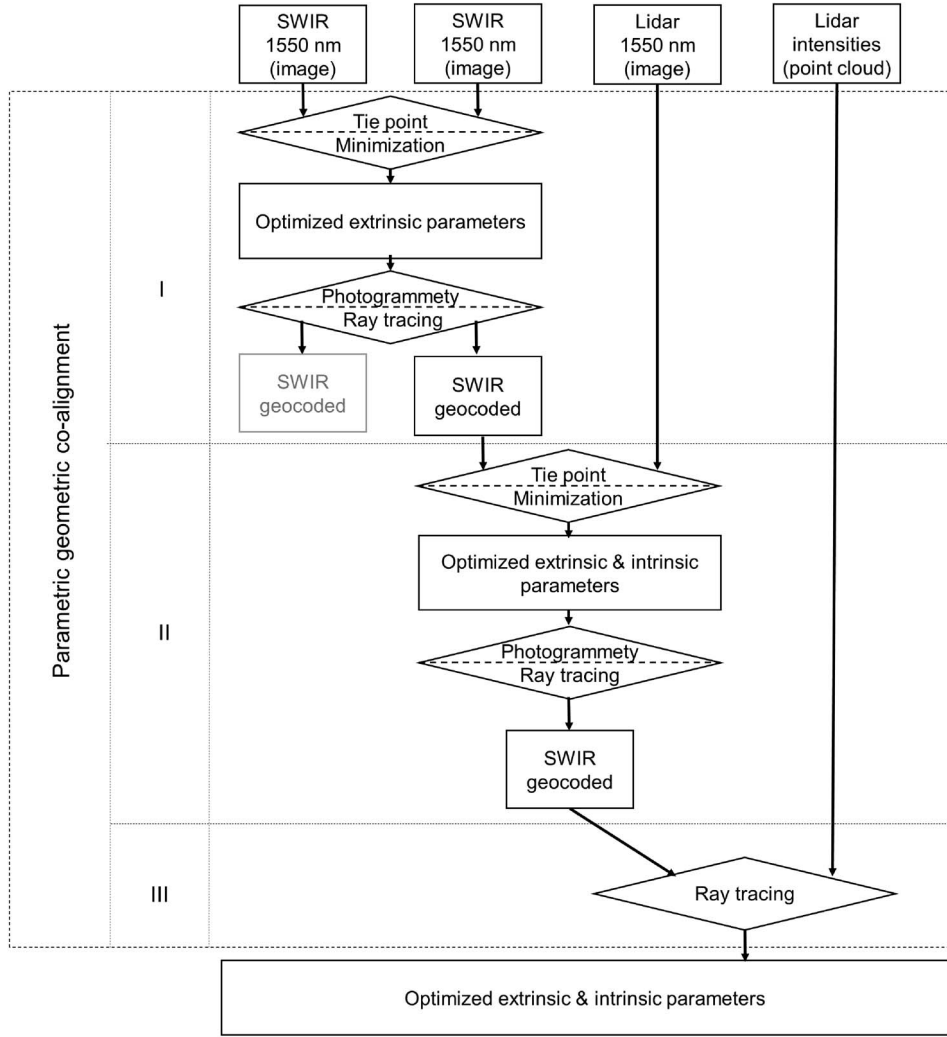
Fig. 6. Detailed workflow of the parametric geometric coalignment procedure divided in three main processing steps. Rectangles represent data products. Rhombs indicate the applied main processing modules (see Fig. 5).

center wavelength of the lidar was directly interpolated with a Hermite spline. A convolution with the expected SRF of the lidar was not performed.

b) Spatial response adaptation: For the spatial response adaptation, the lidar intensity information is adapted spatially to the HSI intensities (1550 nm) (see rhomb 4 in Fig. 2). Two different methods are applied in the coregistration approach. The normal raster-based convolution is described as follows. In addition to this technique, a dynamic ray-tracing-based spatial response adaptation is also realized (see Section III-B2c). The spatial impulse response of an imaging sensor to a point source can be expressed by the point spread function (PSF). The PSF is defined by, among other parameters, the sensor's electronic, detector, optic, and motion characteristics. The lidar intensity data are resampled from the irregular point information to the prospective grid resolution of the geocoded HSI data (1.5 m). Beyond the resolution, the PSF of the hyperspectral sensor is considered by convolving the lidar intensities with an approximated PSF using a Gaussian 2-D function of the HSI sensor. This normal raster-based convolution is realized as a first guess and makes the lidar intensity raster spatially comparable to

the hyperspectral data, whereas the ray tracing approach (see Section III-B2c) is realized for the final refinement. Both spatial response adaptations depend on sufficiently high lidar point density.

2) Parametric Geometric Coalignment: The parametric geometric coalignment (rhomb 6 in Fig. 2) is based on three processing steps. Fig. 6 represents the detailed workflow of this parametric geometric coalignment.

a) Boresight calibration of overlapping hyperspectral images: In the first step, a boresight calibration of hyperspectral images is realized. Therefore, robust tie points are generated between the overlapping areas of preliminary geocoded HSI flight stripes (band 1550 nm) using the described tie-point matching algorithm. These tie points are utilized inside the cost-function minimizer, realizing a first approximation of the SWIR sensor boresight. The photogrammetry processor, in combination with the ray tracing module, assigns the respective coordinates by calculating the intersections between the pointing of the sensor element and the lidar point cloud for the intervals. The boresight variation causing the smallest RMSE between the tie points determines the boresight angle offsets. All HSI SWIR

This article has been accepted for inclusion in a future issue of this journal. Content is final as presented, with the exception of pagination.

BRELL *et al.*: IMPROVING SENSOR FUSION: PARAMETRIC METHOD FOR GEOMETRIC COALIGNMENT OF DATA

9

images are geocoded again using the corrected attitude angles and lidar elevation information.

b) Parametric coregistration of HSI to lidar intensity image: The second step is the tie-point-based parametric coregistration. For every geocoded hyperspectral flight stripe, we generate an intensity image (1550 nm) of the overlapping lidar point cloud (see Section III-B1b). Tie points are generated automatically based on both overlapping intensity grids. The parametric coregistration procedure is also based on the cost-function minimizing module. Subsequently, the refinement of the boresight parameter, i.e., a camera resectioning, is performed with the same minimizing approach. The camera resectioning encompasses the focal length (f) and the principal point (X0a, Y0a) of the SWIR HySpex sensor. All in all, eight parameters (roll, pitch, heading, X0a, Y0a, f, synchronization timing Δt, and altitude) are adjusted with the cost-function minimization module to optimize the accuracy of the coalignment. Table II gives an overview of the considered parameters and in which coalignment step they are optimized (symbolized by the crosses).

At most, three variables are optimized together. Correlated variables are optimized separately. The colors in the table indicate the grouping of parameters optimized together. The complete coregistration procedure can be repeated iteratively if necessary.

c) Ray-tracing-based coalignment of back-projected lidar intensities to HSI lines: The fine ray-tracing-based coalignment of HSI lines and Lidar intensity data is realized in a third step. The final optimization is realized with an area-based approach by back projecting the lidar intensities to the geometric uncorrected HSI intensities. The minimization of the RMSE between a few tie points for different parameters is not a simple linear description of the planar alignment of the HSI with the lidar reference. An area-based cost aggregation method was developed to refine the offset parameter determination (see Fig. 7).

For every pixel of a geometric uncorrected HSI image line (x, n), the corresponding lidar intensity points were collected with the standard ray tracing module. Thus, *the lidar points inside the cone representing the pointing of the corresponding HSI pixel* and their distance to the cone center is calculated. This is done iteratively for small parameter variations (ΔP) for every HSI pixel using the latest optimized parameters from the previous step and for three selected adjacent image lines (n) that are less affected by shadowing. All intensity values of the collected points inside a pixel beam were weighted with Gaussian PSF centered along the center axes of the respective HSI cone. Therefore, the spatial response function is correctly approximated in terms of the spatial footprint projection and orientation of the HSI spatial pointing to the surface. For every parameter iteration step, a convolution with a Laplace kernel is calculated in across-track direction (x) for the respective three adjacent HSI and corresponding lidar intensities. The three lines of the geometrically uncorrected HSI image serve as the template (I_T). The generated corresponding lidar intensities (I_L) for varying parameters (see Table II) are compared with the HSI template by calculating the zero mean sum of squared distance (ZSSD). The offset parameter combination, which
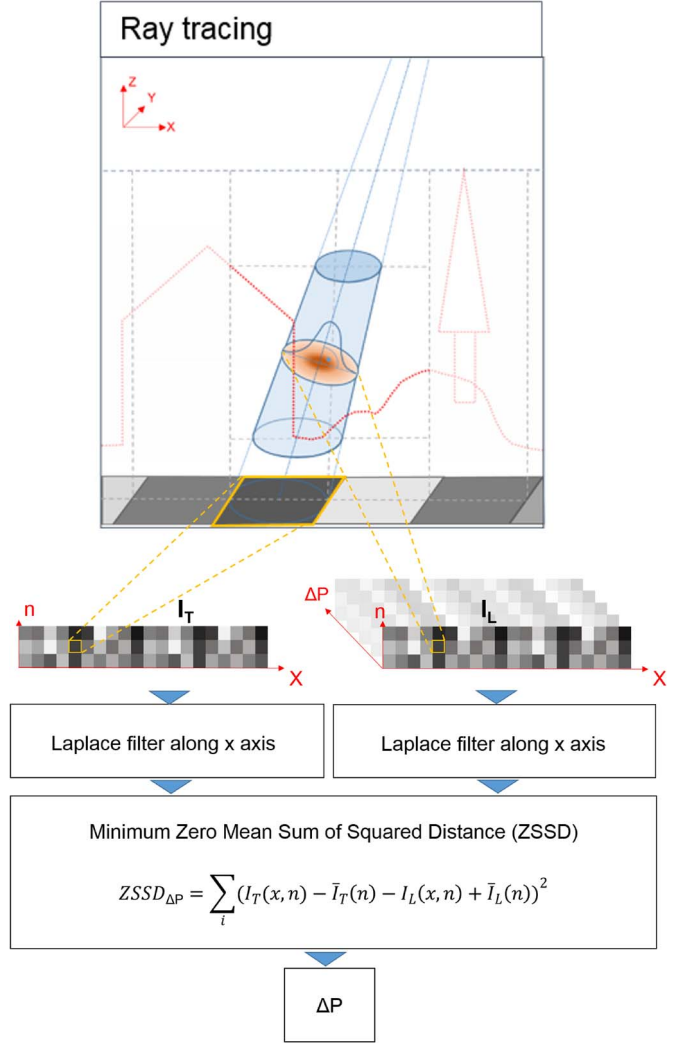

Fig. 7. Ray-tracing-based refinement of the coalignment; I_T (Intensity template) = three HIS intensity image rows (x = across-track direction, n = along-track direction); I_L (Intensity lidar) = corresponding lidar intensities are generated by ray-tracing-based back projection for different offset parameters (ΔP); the ZSSD is calculated between all Laplacian filtered I_L images and the I_t image for every offset parameter variation (ΔP).

generates the match with the smallest ZSSD, is applied globally to refine the geometric correction.

C. Geometric Correction

Provided that the sensor integration and the sensor model are stable during the flight campaign, the determined offset parameters are valid for all acquired flight stripes. Thus, the final procedure is the global assignment of the determined offset parameters to the trajectories and their corresponding SWIR flight stripes. The offset parameters are used inside the photogrammetric processor and the ray tracing module (see Section III-B) for all flight stripes. Although the coalignment of the VNIR sensor to the SWIR sensor can be realized with the same introduced coalignment workflow, the spectral and spatial adaptation methods represented in Section III-B1 with the respective sensor parameters and the same parametric coregistration procedure as represented in Section III-B2 can

This article has been accepted for inclusion in a future issue of this journal. Content is final as presented, with the exception of pagination.

10

IEEE TRANSACTIONS ON GEOSCIENCE AND REMOTE SENSING
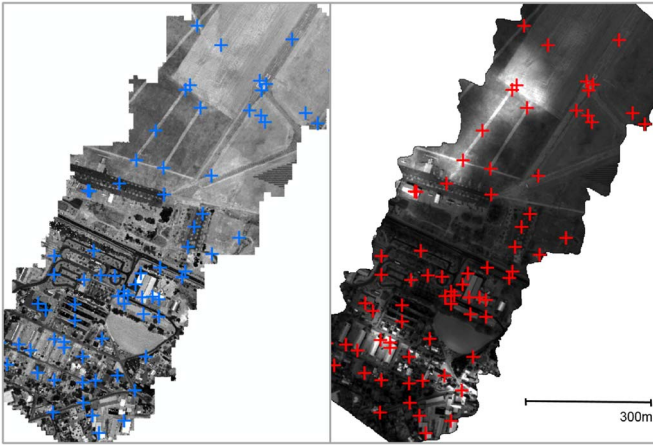

Fig. 8. Accuracy assessment based on 73 manually created tie points: (left) lidar intensity image and (right) HSI intensity image.

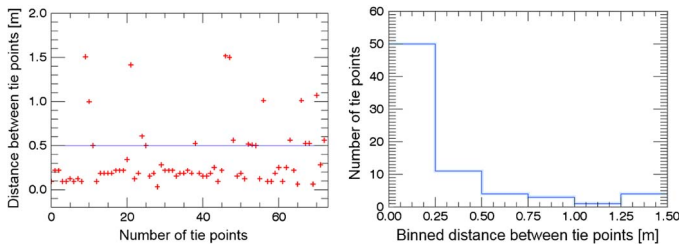Fig. 9. Euclidian distances between related tie points: (left) blue plot represents the RMSE; (right) distance histogram.
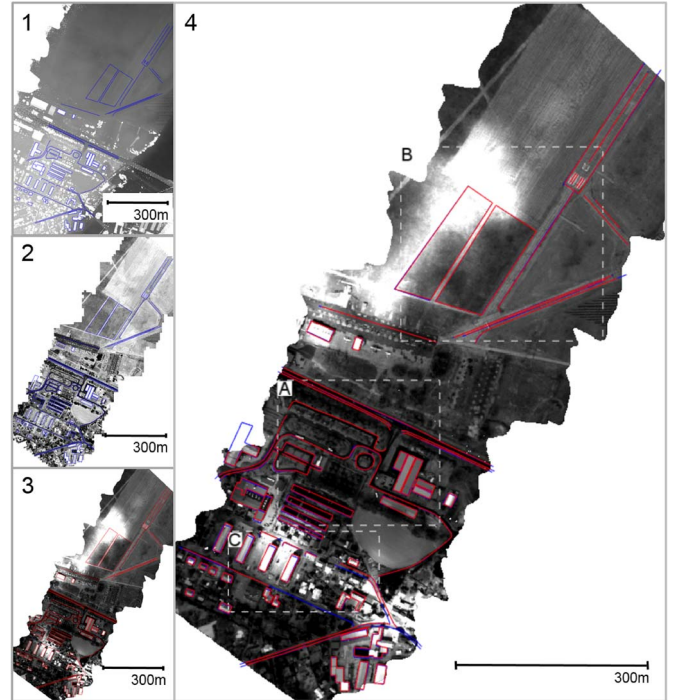

Fig. 10. Overview of accuracy assessment based on delineated structures for subjective evaluation. Structures (blue lines) delineated from 1) a 1-m digital surface model and 2) lidar intensities (1550 nm). 3) Structures (red lines) delineated from orthorectified SWIR (1550 nm) HSI intensity images. 4) Overlay of delineated structures representing the accuracy of geometric description of surface objects. In places where only blue lines (lidar intensity features) without corresponding red lines (HSI intensity features) are visible, the delineation was not possible due to shadowing effects.

be used. However, as a coregistration reference, the already coregistered and spectrally overlapping SWIR band of ∼979 nm can be used.

IV. RESULTS AND DISCUSSION

The introduced geometric coalignment procedure is applied to the data of the conducted calibration flight campaign. It results in a coregistered orthorectified HSI image cube (SWIR), the determined intrinsic sensor parameter, positioning and attitude offsets, and an image geometry map (IGM) file containing the georeferencing information and height information for each HSI image pixel. In addition, a lidar point LUT is generated, which allocates all lidar points falling into an HSI pointing.

For our test flight, the accuracy assessment of the coalignment is realized by a geometric comparison of the coaligned HSI SWIR intensity image with the lidar intensity image. In addition, a short comparison to other related methods is given.

A. Comparison of HSI and LIDAR Intensities

The first accuracy assessment is based on a manually measured set of 73 regularly distributed tie points (see Fig. 8). They result in an RMSE of 0.499 m in the XY direction (RMSE of 0.224 m in X and RMSE of 0.446 m in Y direction). Both intensity images have a grid size of 1.5 m per pixel that leads to an RMSE of less than 1/3 of the grid size. Fig. 9 shows the Euclidian distances between related tie points and the histogram

of these distances. 85% local planar offsets are smaller than the RMSE. Only a few points (15%) have larger offsets that are up to 1.5 m. This indicates high accuracy and precision of the global alignment between lidar intensity image and HSI intensity image.

Tie-point-based accuracy assessment gives only limited information about coalignment accuracy of complex object structures. A visual feature assessment allows for a better local evaluation basis. The indication of how accurate certain structures in HSI fit to the lidar intensity structures is very important for the overall fusion process. The accuracy of the geometric feature fit is essential for extended classifications of surface objects, particularly in spatial and spectral heterogeneous areas. Therefore, a second accuracy assessment was performed, where perceptible linear structures along roads or around building structures were delineated in both intensity images. Fig. 10 gives an overview of the delineated structures, which indicates the global fit of the orthorectified HSI to the lidar intensity. Most of the delineated features exactly overlay along their entire extent. Influences of the stronger perspective distortions toward off-nadir across track are not perceptible. This influences are distinctive for a FOV of about 27.2° and a flight altitude of about 800 m above ground.

A detailed visual assessment (see Fig. 11) and mathematical assessment (see Fig. 12) confirm and refine the result of the overview. Most of the object structures are represented geometrically accurate with subpixel accuracy. Along the structures
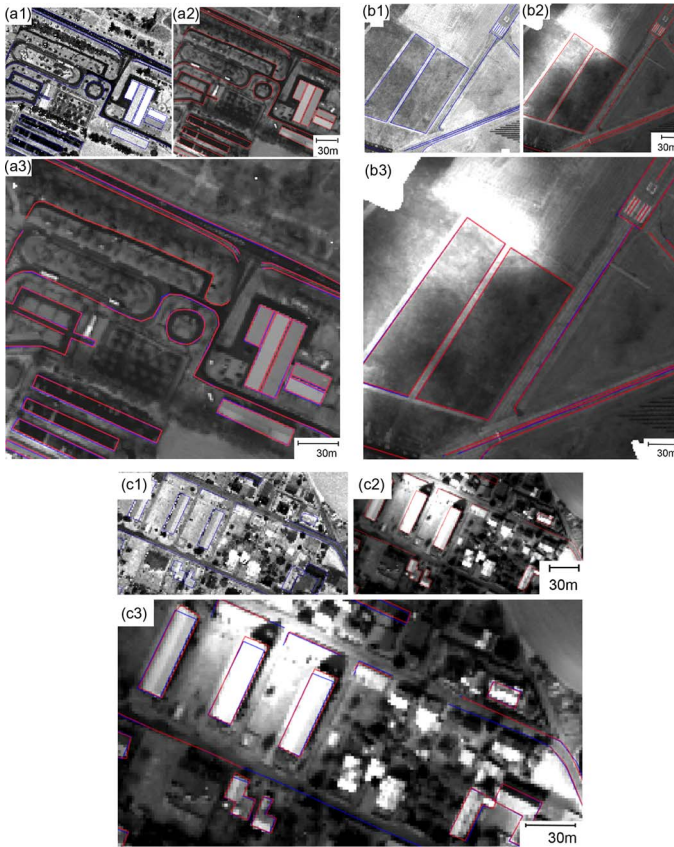
Fig. 11. (a)–(c) Detailed assessment of delineated surface structures for three different areas (see Fig. 9 for location): 1) blue delineated structures based on lidar intensities (1550 nm); 2) red delineated structures based on SWIR HSI intensities (1550 nm); 3) overlaid delineated structures.
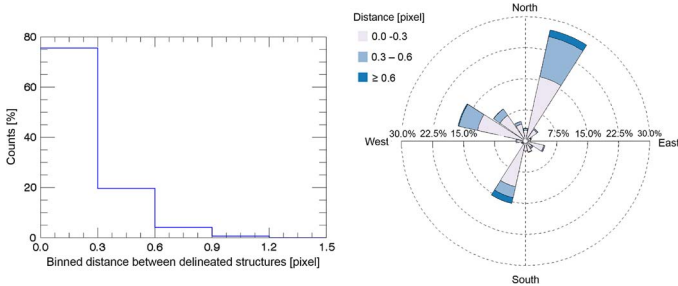

Fig. 12. (Left) Histogram of the Euclidian distances between structures delineated from SWIR intensities (red lines in Fig. 10) and structures from lidar intensities (blue lines in Fig. 10). (Right) Direction dependence of these Euclidian distances represented by a wind rose diagram.

have a Euclidian distance toward the delineated lidar structures that is smaller than 0.6 pixel. The direction dependence is evaluated with the wind rose diagram (right). Overall, the direction dependence is closely bundled to the main orientation of the delineated structures. Most of the structures are orientated along the axis north-northeast south-southwest and west-northwest east-southeast. These orientations are clearly represented inside the wind rose. However, about 28% offsets are in the north-northeast direction, and only about 15% offsets are in the south-southwest direction. This north-northeast trend of accumulation, as well as the tendency of larger offset distances in this direction, can be attributed to some extent to the shadowing of the objects in the HSI intensities. However, the same trend is also visible for the second main axis in the west-northwest direction. This cannot be attributed to shadowing effects and gives an indication for still remaining but very small systematic errors inside the parametric coalignment procedure. However, the delineation accuracy assessment and their diagrams suggest that most of the significant systematic errors inside the coalignment procedure are successfully minimized.

Feature-based methods and intensity-based methods strongly rely on the image quality. In particular, nonparametric methods need homogeneous distributed image features and homogeneous illumination all over the image. The shadowing effects in the HSI images and the different spatial responses of both sensors have been the major challenges for a proper coregistration. The represented coregistration algorithm has proven to have the potential to overcome both problems through carefully chosen parameters. Thus, the determined offset parameters (see Table II) are applicable for a complete data acquisition campaign. Despite the clearly perceptible nonoptimal illumination conditions due to object and cloud shadowing (Fig. 10), an accurate automatic coregistration was performed. The shadows were problematic during the visual accuracy assessment, and it was difficult to visually differentiate between object boundaries and object shadows. The normalized difference image (see Fig. 13) gives an overview of the illumination differences between lidar and HSI. The absolute normalized difference image shows more heterogeneous patterns, particularly in the urban area, which are introduced by the reflection properties and the exposer of different surface features, but also the variation of laser penetration rates into vegetation leads to significant differences [37]. However, image gradients around objects, which would be introduced by geometric misregistrations, are not perceptible inside the normalized difference images. All spatial patterns introduced by intensity differences can be attributed to illumination and reflectance issues of the surface objects. The difference images should only give an idea of the diverse intensity responses and how they can be attributed. The differences should not be overinterpreted, due to the fact that the lidar intensities are not radiometrically calibrated.

The workflow results from the challenging differences of the spatial and spectral responses. It is not possible to generate enough robust tie points between the adopted lidar intensity image and the HSI image data, before the first coarse geometric coalignment of the HSI overlapping flight stripes. Only the coarse geometric coalignment of the HSI overlapping flight stripes and the spectral and spatial adaptation allows for the

of the flat terrain of the flight field [see Fig. 11(b)] and the roads, the delineations match perfectly. In addition, the building structures shown in Fig. 11(a) and (c) are aligned very accurately. Only the buildings in parallel have a clearly perceptible foreshortening of 1–2 pixels in the along-track direction, which could not be assigned to the determined offset parameters [see Fig. 11(c)]. This effect can be caused, for example, by nonlinearities in the synchronization timing or position and attitude accuracies. Fig. 12 shows diagrams of the shortest Euclidian distance between the delineated lidar structures and 215 885 points generated along the delineated SWIR structures. The histogram (left) shows that more than 95% of the points
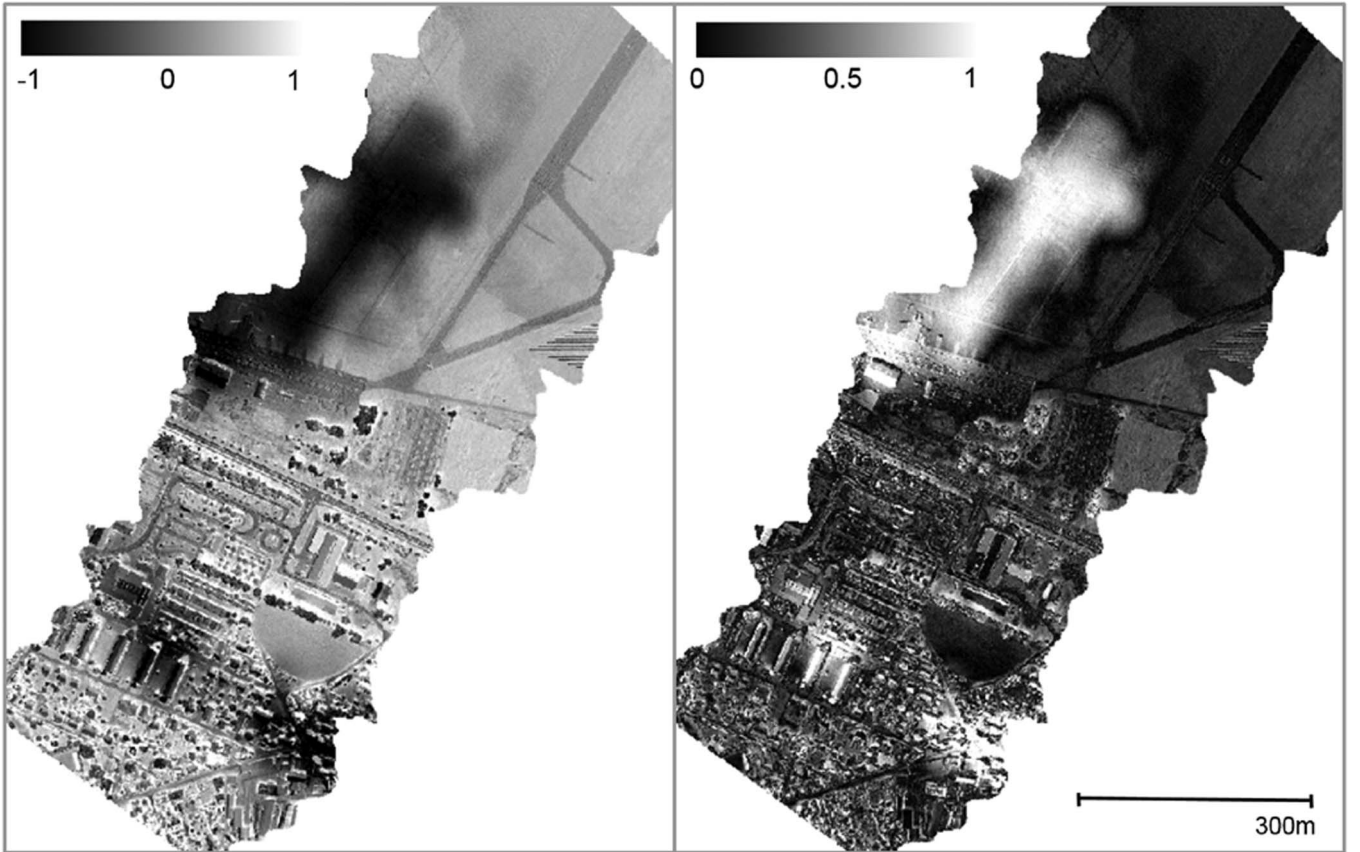
Fig. 13. (Left) Normalized difference image and (right) absolute normalized difference image between lidar intensities and HSI intensities. Both intensity images were normalized to values between 0 and 1 by their respective maximum intensities. The normalized HSI intensities were subtracted from the normalized lidar intensities. In the normalized difference image (left), gray areas represent less difference between lidar and HSI. White areas represent the illumination differences introduced by shadowing objects. Black areas represent cloud gaps introducing high intensities in the HSI images. In the absolute normalized difference image (right), black areas represent intensity differences close to zero.

automatic tie-point matching between HSI and lidar intensities. For this purpose, 214 robust tie points were detected between the overlapping SWIR HSI flight lines (see Section III-B2a). The boresight determination starts at an RMSE of 50 m (boresight offsets propagate in different directions due to apposed flight lines) and results after nine iterations in an RMSE of 2.497 m (see left in Fig. 14) between the overlapping SWIR HSI flight lines. Boresight offsets of $-1.638°$ for roll, $0.618°$ for pitch, and $0.290°$ for heading were detected. Additional iterations did not improve the RMSE.

For the parametric coregistration of the HSI image to the lidar intensity image, 41 tie points were generated. At the beginning, a misregistration with an RMSE of 3.198 m between HSI and lidar images was measured. The optimization of roll, pitch, and heading leads to an RMSE of 1.938 m (seem middle in Fig. 14). The additional optimization of focal length, principal point, synchronization timing, and altitude leads to an improvement of the RMSE to 1.169 m (see right in Fig. 14).

An iteration of the complete tie-point-based parametric coregistration (see Section III-B2b) did not lead to perceptible alignment improvements. However, the ray-tracing-based cost aggregation of complete sensor lines (see Section III-B2c) leads to improvement in alignment accuracy. The global accuracy and precision is improved, but in particular, the local object
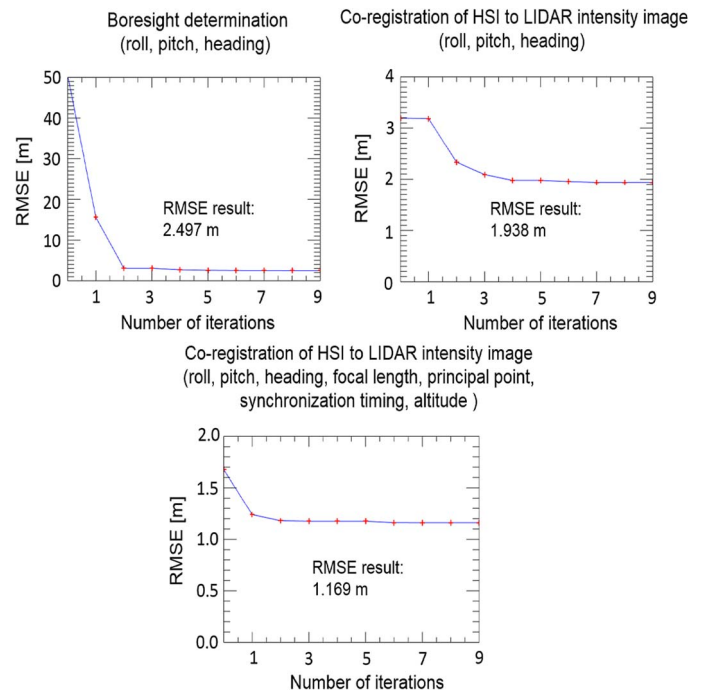

Fig. 14. RMSE optimization using the sequenced geometric alignment procedures.

This article has been accepted for inclusion in a future issue of this journal. Content is final as presented, with the exception of pagination.

BRELL *et al.*: IMPROVING SENSOR FUSION: PARAMETRIC METHOD FOR GEOMETRIC COALIGNMENT OF DATA 13

structure alignment gains form the area-based refinement. The stability of the algorithm is influenced to some extent by the different shading characteristics that are inherent between both images and by the point density of the lidar. Therefore, lines with less shadowing influence should be chosen for the refinement of the coregistration. The final back projection based on ray tracing results in parameter offsets of $-1.817°$ for roll, $0.461°$ for pitch, $0.231°$ for heading, 0.251 m for the altitude, 0.033 s for synchronization time (Δt), -0.680 pixel for the focal length (f), and for the principle point -0.607 (X0a) and 0.178 (Y0a).

The adaptation of the overlapping spatial and spectral domains is a requirement for the comparison of both sensor entities with subpixel accuracy. Sufficient tie points can be generated between HSI and lidar intensity images also for off-nadir areas influenced by stronger perspective distortions. The combination of the robust feature detector SIFT, the sensor specific feature matching, and the final perspective transformation model (homography)-based outlier removal (RANSAC) results in a very robust tie-point detection and matching algorithm. The used minimization procedure is based on computationally costly and slow forward projection and bisectioning. However, the results appear to be very robust for the parameter minimization incorporating the ray-tracing-based height determination. Improving the rate of convergence by using gradient minimization techniques appeared less robust than minimizing the pure cost-function value based on bisectioning.

For achieving subpixel accuracy, it is necessary to accomplish all processing steps on the original temporal resolution of the preprocessed navigation file. A discretization into integral rows, particularly during the parametric minimization procedures, results in a RMSE of only 2/3 of the grid resolution (instead of 1/3 of the grid resolution). The rigorous parametric geocoding procedure incorporates the geometric and spectral sensor model. However, it proves to be very effective to optimize the HSI intrinsic sensor additional to the exterior parameter. Therefore, geometric sensor variations can be compensated in relation to the determined sensor model.

B. Comparison to Related Methods

For a comparison to related methods, the HSI data were also coregistered to the lidar intensity image by using the common HSI direct geocoding software PARGE [11]. Therefore, a parameter optimization of roll, pitch, heading, and altitude was realized based on 27 manually generated and iteratively filtered tie points. This procedure only leads to an RMSE of 3.03 m (about 2 pixels) measured based on 22 independent manually set tie points. This can be only understood as a rough and partially comparison, but it indicates the efficiency of the comprehensive proposed method and that a common tie-point-based boresight alignment does not eliminate all inherent systematic errors. Additional sensor-driven parametric coregistration methods were not available within the study. A comparison with a feature-based rubber-sheeting method is obviously not a good solution, due to its nonparametric character and, therefore, the associated lack of generalization and repeatability for different surface structures and acquisition conditions. Therefore, the presented results can only be theoretically dis-

cussed and compared with published and adequate coalignment techniques. Asner *et al.* [1] introduced the most comparable approach. With their parametric coalignment that is completely tie-point based, they achieved accuracies of "$\ll 1$ pixel RMSE." However, they described the geometric alignment in a more general manner. Despite the lack of the presented ray-tracing-based back projection and a missing accuracy assessment based on delineated features, the theoretical comparison indicates that the achieved results are appropriate. In addition, the acquisition conditions, sensor design, sensor calibration, and sensor integrations differ between the different studies; hence, it is very difficult to make a theoretical and reliable comparison. We emphasize that most published papers focus only on the accuracy assessment of retrieved information from the combination of both data entities and not on the geometric coalignment. Therefore, this is the first study explicitly focusing on the methodology of intensity-based in-flight parametric coregistration between these two sensors types.

This research indicates that one coalignment approach on its own is not sufficient for an accurate coalignment between the heterogenic sensors. The stepwise accuracy improvement realized by the introduced three-step alignment approach shows the evidence of using complementary fundamental and advanced coregistration strategies as well as sensor-driven spatial response adaptation techniques beyond standard tie-point-based approaches also inside parametric approaches. The presented parametric coalignment approach has the advantage over nonparametric methods that locally derived parameters could be assigned to the global flight campaign independent from local illumination conditions and detectable surface structures. Additionally, the optimization of eight extrinsic and intrinsic parameters makes the method robust against changes of the sensor model. The approach of parametric compensation of systematic alignment errors between the sensors and its consequent generic sensor-driven design guarantees that the method is highly repeatable and generalizable. The point-feature-based algorithm is suitable to match hyperspectral pushbroom sensors and lidar intensity data with subpixel precision. Nevertheless, the alignment accuracy improvements caused by the area-based refinement indicate that the point-based approach did not completely characterize the coalignment. The hybrid coalignment strategy (point-feature-based RMSE and area-based cost aggregation) overcomes the drawbacks of the respective methods. Overall, the ray tracing approach based on lidar point data enables the highest accuracy concerning elevation integration and spatial intensity adaptation. It establishes the development of further geometric coalignment refinement procedures on a vector base. Both approaches in combination allow for coalignment possibilities without discretization and thus minimize radiometrically relevant resampling errors.

V. SUMMARY

In this paper, we have presented a parametric physical-based geometric coalignment of HSI to lidar intensity data. It is shown that the lidar data help to improve the accuracy and precision of georeferenced hyperspectral data, in addition to adding elevation information.

The presented hybrid coalignment methods is based on three processing steps. In a first step, a coarse boresight alignment between overlapping hyperspectral flight stripes is realized. Second, a tie-point-based parametric coalignment of hyperspectral to lidar intensities is performed. The optimization includes extrinsic and intrinsic hyperspectral sensor parameters. The third step is a parametric coalignment refinement utilizing an area-based cost aggregation between overlapping hyperspectral to lidar intensities. The combination of diverging alignment procedures is necessary because of different sensor responses. It is shown that a ray-tracing-based back projection of the lidar point intensities and their spatial response adaptation to the geometric uncorrected HSI intensities ensures a subpixel accuracy which is superior to conventional tie-point-based approaches. A tie-point-based coalignment by itself is not sufficient to describe the overall geometric accuracy of the alignment. The area-based cost aggregation, however, is able to compensate these lacks and increases the geometric alignment accuracy. Altogether, it is advisable to optimize the intrinsic parameters of the HSI sensors additionally to the extrinsic offset parameters to reduce the entire error budget of the coalignment. The lidar point intensity, as well as the elevation information, has the potential to stabilize the geometric preprocessing workflow at least for relatively flat but heterogeneous terrain. The fusion of both data entities results in geometrically coaligned data, achieving accuracies of 1/3 pixel with high precision.

Our results indicate that the hybrid utilization of tie-point-based and area-based cost aggregation appears to be very promising. The approach provides the basis for a comprehensive physical fusion of hyperspectral and lidar data.

REFERENCES

[1] G. P. Asner *et al.*, "Carnegie Airborne Observatory-2: Increasing science data dimensionality via high-fidelity multi-sensor fusion," *Remote Sens. Environ.*, vol. 124, pp. 454–465, Sep. 2012.

[2] U. Heiden *et al.*, "Urban structure type characterization using hyperspectral remote sensing and height information," *Landscape Urban Plann.*, vol. 105, no. 4, pp. 361–375, Apr. 2012.

[3] A. Brook, E. Ben-Dor, and R. Richter, "Fusion of hyperspectral images and LiDAR data for civil engineering structure monitoring," in *Proc. 2nd WHISPERS*, 2010, pp. 1–5.

[4] H. Buddenbaum, S. Seeling, and J. Hill, "Fusion of full-waveform lidar and imaging spectroscopy remote sensing data for the characterization of forest stands," *Int. J. Remote Sens.*, vol. 34, no. 13, pp. 4511–4524, Jul. 2013.

[5] T. U. Kampe, B. R. Johnson, M. A. Kuester, and M. Keller, "NEON: The first continental-scale ecological observatory with airborne remote sensing of vegetation canopy biochemistry and structure," *J. Appl. Remote Sens.*, vol. 4, no. 1, Jan. 2010, Art. ID 043510.

[6] B. Koetz *et al.*, "Fusion of imaging spectrometer and LIDAR data over combined radiative transfer models for forest canopy characterization," *Remote Sens. Environ.*, vol. 106, no. 4, pp. 449–459, Feb. 2007.

[7] M. Dalponte, L. Bruzzone, and D. Gianelle, "Fusion of hyperspectral and LIDAR remote sensing data for classification of complex forest areas," *IEEE Trans. Geosci. Remote Sens.*, vol. 46, no. 5, pp. 1416–1427, May 2008.

[8] M. Alonzo, B. Bookhagen, and D. A. Roberts, "Urban tree species mapping using hyperspectral and lidar data fusion," *Remote Sens. Environ.*, vol. 148, pp. 70–83, May 2014.

[9] B. Cook *et al.*, "NASA Goddard's LiDAR, Hyperspectral and Thermal (G-LiHT) Airborne Imager," *Remote Sens.*, vol. 5, no. 8, pp. 4045–4066, Aug. 2013.

[10] G. P. Asner *et al.*, "Carnegie airborne observatory: In-flight fusion of hyperspectral imaging and waveform light detection and ranging for three-dimensional studies of ecosystems," *J. Appl. Remote Sens.*, vol. 1, no. 1, Sep. 2007, Art. ID 013536.

[11] D. Schläpfer and R. Richter, "Geo-atmospheric processing of airborne imaging spectrometry data. Part 1: Parametric orthorectification," *Int. J. Remote Sens.*, vol. 23, no. 13, pp. 2609–2630, Jan. 2002.

[12] E. P. Baltsavias, "A comparison between photogrammetry and laser scanning," *ISPRS J. Photogramm. Remote Sens.*, vol. 54, no. 2/3, pp. 83–94, Jul. 1999.

[13] R. Muller *et al.*, "A program for direct georeferencing of airborne and spaceborne line scanner images," in *Proc. Int. Arch. Photogramm. Remote Sens. Spatial Inf. Sci.*, 2002, vol. 34, pp. 148–153.

[14] R. Richter and D. Schläpfer, "Geo-atmospheric processing of airborne imaging spectrometry data. Part 2: Atmospheric/topographic correction," *Int. J. Remote Sens.*, vol. 23, no. 13, pp. 2631–2649, Jan. 2002.

[15] H. Torabzadeh, F. Morsdorf, and M. E. Schaepman, "Fusion of imaging spectroscopy and airborne laser scanning data for characterization of forest ecosystems—A review," *ISPRS J. Photogramm. Remote Sens.*, vol. 97, pp. 25–35, Nov. 2014.

[16] J. Avbelj, D. Iwaszczuk, R. Müller, P. Reinartz, and U. Stilla, "Coregistration refinement of hyperspectral images and DSM: An object-based approach using spectral information," *ISPRS J. Photogramm. Remote Sens.*, vol. 100, pp. 23–34, Feb. 2015.

[17] J. Lee, X. Cai, C.-B. Schonlieb, and D. A. Coomes, "Nonparametric image registration of airborne LiDAR, hyperspectral and photographic imagery of wooded landscapes," *IEEE Trans. Geosci. Remote Sens.*, vol. 53, no. 11, pp. 6073–6084, Nov. 2015.

[18] D. Schlapfer, J. Nieke, and K. I. Itten, "Spatial PSF nonuniformity effects in airborne pushbroom imaging spectrometry data," *IEEE Trans. Geosci. Remote Sens.*, vol. 45, no. 2, pp. 458–468, Feb. 2007.

[19] M. T. Eismann, *Hyperspectral Remote Sensing*. Bellingham, WA, USA: SPIE, 2012.

[20] R. A. Schowengerdt, *Remote Sensing: Models and Methods for Image Processing*. San Diego, CA, USA: Academic, 2006.

[21] L. Guanter *et al.*, "Scene-based spectral calibration assessment of high spectral resolution imaging spectrometers," *Opt. Exp.*, vol. 17, no. 14, pp. 11 594–11 606, Jul. 2009.

[22] C. Rogass, M. Brell, K. Segl, T. Kuester, and H. Kaufmann, "Automatic reduction of keystone applications to EnMAP," in *Proc. 8th EARSeL SIG Imaging Spectrosc. Workshop*, Nantes, France, 2013.

[23] A. Wehr and U. Lohr, "Airborne laser scanning—An introduction and overview," *ISPRS J. Photogramm. Remote Sens.*, vol. 54, no. 2/3, pp. 68–82, Jul. 1999.

[24] E. P. Baltsavias, "Airborne laser scanning: Basic relations and formulas," *ISPRS J. Photogramm. Remote Sens.*, vol. 54, no. 2/3, pp. 199–214, Jul. 1999.

[25] P. Gege *et al.*, "Calibration facility for airborne imaging spectrometers," *ISPRS J. Photogramm. Remote Sens.*, vol. 64, no. 4, pp. 387–397, Jul. 2009.

[26] A. Baumgartner, P. Gege, C. Köhler, K. Lenhard, and T. Schwarzmaier, "Characterisation methods for the hyperspectral sensor HySpex at DLR's calibration home base," in *Proc. SPIE Remote Sens.*, 2012, p. 85331H.

[27] K. Lenhard, A. Baumgartner, and T. Schwarzmaier, "Independent laboratory characterization of NEO HySpex imaging spectrometers VNIR-1600 and SWIR-320m-e," *IEEE Trans. Geosci. Remote Sens.*, vol. 53, no. 4, pp. 1828–1841, Apr. 2015.

[28] L. Guanter, K. Segl, and H. Kaufmann, "Simulation of optical remote-sensing scenes with application to the EnMAP hyperspectral mission," *IEEE Trans. Geosci. Remote Sens.*, vol. 47, no. 7, pp. 2340–2351, Jul. 2009.

[29] HySpex, Norsk Elektro Optikk, Accessed on: May 19, 2015. [Online]. Available: http://www.hyspex.no/index.php

[30] RIEGL—RIEGL Laser Measurement Systems, Accessed on: May 19, 2015. [Online]. Available: http://www.riegl.com/

[31] C. Rogass *et al.*, "Reduction of uncorrelated striping noise—Applications for hyperspectral pushbroom acquisitions," *Remote Sens.*, vol. 6, no. 11, pp. 11082–11106, Nov. 2014.

[32] D. G. Lowe, "Distinctive image features from scale-invariant keypoints," *Int. J. Comput. Vis.*, vol. 60, no. 2, pp. 91–110, Nov. 2004.

[33] M. A. Fischler and R. C. Bolles, "Random sample consensus: A paradigm for model fitting with applications to image analysis and automated cartography," *Commun. ACM*, vol. 24, no. 6, pp. 381–395, Jun. 1981.

[34] K. Segl *et al.*, "EeteS—The EnMAP end-to-end simulation tool," *IEEE J. Sel. Topics Appl. Earth Observ. Remote Sens.*, vol. 5, no. 2, pp. 522–530, Apr. 2012.

[35] D. Schläpfer, A. Boerner, and M. Schaepman, "The potential of spectral resampling techniques for the simulation of APEX imagery based on AVIRIS data," in *Proc. Summaries 8th JPL Airborne Earth Sci. Workshop*, Pasadena, CA, USA, 1999, vol. 99, pp. 377–384.

[36] C. Rogass, K. Segl, C. Mielke, Y. Fuchs, and H. Kaufmann, "EnGeoMap—A geological mapping tool applied to the EnMAP mission," in *Proc. EARSeL*, 2014, vol. 12, pp. 94–100.

[37] M. Alonzo, B. Bookhagen, J. P. McFadden, A. Sun, and D. A. Roberts, "Mapping urban forest leaf area index with airborne lidar using penetration metrics and allometry," *Remote Sens. Environ.*, vol. 162, pp. 141–153, Jun. 2015.

Maximilian Brell received the Diploma in geography from the Dresden University of Technology, Dresden, Germany, in 2011. He is currently working toward the Ph.D. degree with the Helmholtz Centre Potsdam GFZ German Research Centre for Geosciences, Potsdam, Germany, where he has been writing his thesis in the field of airborne hyperspectral imaging and LiDAR sensor fusion since mid-2013.

After a short period in the private sector, he served as a Research Assistant with the Remote Sensing Section, Helmholtz Centre Potsdam GFZ German Research Centre for Geosciences. He developed a preprocessing chain for airborne hyperspectral data.

Christian Rogass received the Diploma in geodesy from the Dresden University of Technology, Dresden, Germany, in 2003 and the Ph.D. degree (Dr.-Ing.) from the Brandenburg University of Technology, Cottbus, Germany, in 2009.

He is a Postdoctoral Researcher with the Helmholtz Centre Potsdam GFZ German Research Centre for Geosciences, Potsdam, Germany. His research interests include sensor systems, imaging spectroscopy, pattern recognition, and geological applications.

Karl Segl received the Ph.D. degree from the University of Karlsruhe, Karlsruhe, Germany, in 1996.

He is currently a Senior Scientist with the Helmholtz Centre Potsdam GFZ German Research Centre for Geosciences, Potsdam, Germany, in the Remote Sensing Section. He has more than 20 years of experience in the field of imaging spectroscopy, and he teaches remote sensing at the University of Potsdam, Potsdam. His research interests focus on new methodological developments for hyperspectral data analysis, sensor design, and validation.

Bodo Bookhagen received the Diploma in geology and the Ph.D. degree in geoscience (summa cum laude) from the University of Potsdam, Potsdam, Germany, in 2000 and 2005, respectively.

He was a Postdoctoral Researcher with the University of California at Berkeley (UC Berkeley), Berkeley, CA, USA; Stanford University, Stanford, CA; and UC Santa Barbara. During 2007–2014, he was an Assistant and Associate Professor with UC Santa Barbara. Since 2014, he has been the Chair of Geological Remote Sensing with the University of Potsdam.

Luis Guanter received the Ph.D. degree in the field of environmental physics from the University of Valencia, Valencia, Spain, in 2007.

He held postdoctoral positions with the Helmholtz Centre Potsdam GFZ German Research Centre for Geosciences (GFZ Potsdam), Potsdam, Germany, and the Freie Universität Berlin, Berlin, Germany, and also with Oxford University, Oxford, U.K., as European Commission (EC) Marie Curie Fellow. Since October 2014, he has served as the Leader of the Remote Sensing Section with the Helmholtz Centre Potsdam GFZ German Research Centre for Geosciences, in a joint appointment professorship position with the Institute of Earth and Environmental Science of the University of Potsdam. He has also been leading the DFG Emmy Noether Junior Research Group on chlorophyll fluorescence monitoring since 2012. His main research interest is the monitoring of land and atmospheric processes through imaging spectroscopy.

Dr. Guanter is the Scientific Principle Investigator of the Environmental Mapping and Analysis Program (EnMAP) hyperspectral mission and a member of the advisory board of other satellite missions.